RESEARCH PAPER

Preparation of Nanohybrid CuO-Fe₃O₄/Zeolite Nanocomposite as Potential Adsorbent for Toxic As (V) and Pb(II) from Water Solution

Abdullah A. Alswat[1],*, Fares T. Al-shorifi[2,3],*, Shaimaa L. Ali[4]

* F.Alshareefi@su.edu.ye

[1] Department of chemistry, Faculty of education and Applied Science- Arhab, Sana'a University, Yemen
[2] Department of chemistry, Faculty of Science, University of Saba region, Marb, Yemen
[3] Department of chemistry, Faculty of Science, Sana'a University, Sana'a, Yemen
[4] Chemistry Department, Faculty of Science, Mansoura University, Mansoura, Egypt

Abstract: In this paper, novel Nanohybrid CuO-Fe₃O₄/Zeolite nanocomposites (HCFZ NCs) were synthesized to improve the adsorption capacity and activity for removing the Arsenic and Lead cations from the contaminated water solutions. The nanohybrid 4, 10, and 20 -HCFZ NC samples were investigated by XRD, FT-IR, TEM, FESEM, EDX, and BET. The characterization results confirmed the presence of CuO and Fe₃O₄ NPs having nanospherical shapes as Nanohybrid Cu and Fe oxides on the zeolite surface. Notably, the 10-HCFZ NC sample showed the highest removal efficiency for harmful metallic pollutants from the water in comparison to the prepared neat zeolite, 4-HCFZ NC, and 20-HCFZ NC samples, with a percentage removal of 97.9% for Pb ions and 93.5% for As ions within 30 minutes (100 ppm). According to the adsorption isotherms results, R^2 values for the Langmuir isotherm were the highest, suggesting that the experimental results fit better the Langmuir isotherm model. Generally, according to the obtained results, there is a possibility of enhancing the efficiency of Nanohybrid CuO-Fe₃O₄/Zeolite NCs to remove Arsenic and Lead ions from polluted aqueous solutions.

Keywords: Zeolite, nanometal oxide, adsorption, nanoparticles, Nanohybrid CuO-Fe₃O₄.

1. INTRODUCTION

Recently, a major current focus in the development of nanomaterials has been well-documented. Nanocomposites (NCs) are striking and reliable nanometals of great concern based on their tendency to incorporate the attainable features of various nanoscales with exceptional and unique features not found in conventional composites [1, 2]. Nano-metal oxides are nanomaterials with novel size and morphology-controlled design and they differ greatly from bulk materials not only in terms of chemical and physical properties but also in terms of their promising applications [3, 4]. Metal oxides catalysts are essential in many chemical and industrial processes due to their role as mediators in oxidation reactions. The catalytic properties of metal oxide NPs can be easily altered by controlling the shape, size, and surface modification of nanomaterials [5–10]. New strategies for the synthesis of metal oxides-supported catalysts have resulted in the development of nano-catalysts with high activity for the removal of pollutants from water solution and for the catalysis of various organic reactions

[8, 11–13]. So, the use of support (MOFs [14, 15], MCM-41 [16, 17], zeolite [18, 19], etc.) could be important for preparing synergistic catalysts which have high efficiency. Nowadays, copper oxide and ferric oxide nanoparticles (CuO and Fe₃O₄ NPs) have been worthwhile studied as sorption materials for removing hazardous metals from aqua systems [20]. However, the agglomeration of nanoparticles (NPs) has been noted as the main drawback that usually limits their vast applications [5]. To address this issue, stabilizers materials, supports, and attachment hosts with a porous structure and large surface area are being developed to support the hybrid nanomaterials and/or the nanometal oxides with surface functionalities for key applications [21]. Apart from that, zeolites are generally crystalline, microporous, eco-friendly in nature, have high thermal stability with a large surface area, with a 1.3 nm cavities diameter, easily tunable, their chemical and physical properties [22], known to be molecular sieves [23] are performing promising hosts and stabilizers [24]. Furthermore, they have a high ion exchange capacity within their dimensions of $[AlO_4]^{5-}$ and $[SiO_4]^{4-}$ tetrahedral due to the substitution of Si^{4+} with Al^{3+}

1

Abdullah A. Alswat, Fares T. Al-shorifi, Shaimaa L. Ali

resulting in a negative charge in the lattice that can probably be neutralized with sodium, calcium, and potassium [25]. Much recent research has been done on the framework of zeolites as template and/or support materials to control the size of nanometals and/or nano-metal oxides for improving the hybrid chemical and physical properties and the potential applications [26]. Haileyesus Tedla et al. reported zeolite-$ZnO/Fe_3O_4/MnO_2$ NCs for photodegradation of both methylene blue (MB) and real sewage [27]. Abdullah A. Alswat et al. prepared zeolite/zinc Oxide NCs [28], zeolite/Fe_3O_4 NCs, and zeolite/CuO NCs and tested their adsorption capacity for removing Arsenic (V) and Lead (II) from aqueous solution [29]. Simin Shokrolahi et al. synthesized a ZnO/Fe_3O_4/zeolite nano-photocatalyst and its performance in the degradation of Enrofloxacin antibiotic in contaminated water [30]. Industrial activities frequently contain a finishing technique that helps generate waste [31]. Heavy metal ions and organic pollutants obtained from these wastes could somehow cause water pollution besides fetal diseases like bone marrow disorder, skin lungs, kidney cancer, and other diseases [32]. The maximum allowable concentrations of Arsenic and Lead cations in potable water are 0.01 mg/L and 0.015 mg/L according to (WHO) guidelines [33]. At least 300 million people worldwide have been drinking water poisoned with Arsenic above 0.01 mg/L, WHO guidelines [34]. Therefore, there is an urgent need to address the problem in operationally easy and cost-effective methods. Adsorption has been outlined as the most profitable and effective technology to remove lead and arsenic from aqua systems [35]. An alternative approach of newer and superior zeolite\nano-metal oxides/or nanohybrid metal oxides is now being developed to monitor the water contamination. However, a nanocomposite made of hybrid CuO-Fe_3O_4 NPs and zeolite has not been reported and tested for the removal of toxic Arsenic and Lead cations. Hence, in this study, close attention is paid to preparing new, promising, and novel x wt.% Nanohybrid CuO-Fe_3O_4/zeolite catalysts to improve the adsorption capacity and activity for removing the Arsenic and Lead cations from the contaminated water solution. Moreover, the prepared HCFZ NC catalysts have been characterized using various techniques; XRD, FT-IR, TEM, FESEM, EDX and BET.

2. EXPERIMENTAL PROCEDURE

2.1. Materials and methods

Acros Organic (USA) and Sigma-Aldrich supplied iron sulphate and iron (III) chloride ($FeCl_3.6H_2O$) (99%), respectively, and Fisher brand supplied $Cu(NO_3)_2.3H_2O$, (Hong Kong). Sigma-Aldrich sells a synthetic zeolite powder with a crystalline structure in sodium form, an effective pore opening of 4 angstroms, and an average particle size of 45 μm. (St Louis, MO, USA). R & M Chemical in the United Kingdom provided 99 % sodium hydroxide (NaOH).

2.2. Synthesis of catalysts

Five grams of zeolite were dispersed in 100 mL of deionized water (DW). Then, appropriate amounts of $FeSO_4$ and $FeCl_3.6H_2O$ with a molar ratio of (1:2) and Cu $(NO_3)_2.3H_2O$ were separately added into zeolite-DW suspension under continuously stirring. The pH of hybrid metals-zeolite suspension after adding Cu and Fe salt solutions was 5.4. The wt.% of Cu and Fe oxides compounds to neat zeolite were (2:2, 5:5, and 10:10%). The hybrid metals-zeolite suspensions were separately stirred under reflux reaction at 80°C for 5 h, in which the Fe^{3+} and Cu^{2+} exchanged zeolite as an ion exchange process. For precipitation of the hybrid Cu and Fe oxides onto the zeolite surface, (2 M) NaOH was added to the hybrid metals-zeolite suspension then stirred until the color turns to black and the pH become 11.0. The resulting slurry was then stirred for another 2 hours. The resulting x wt.% Nanohybrid CuO-Fe_3O_4/zeolite NCs were filtered, thoroughly washed with DW, and dried overnight in an oven at 80°C. Subsequently, the As-prepared x wt% -HCFZ NCs were calcined at 450°C for 3 h, separately. The Nanohybrid CuO-Fe_3O_4/zeolite NCs with different mass ratios of hybrid CuO-Fe_3O_4 (2:2 wt. %, 5:5 wt.%, and 10:10 wt.%) on the zeolite as 4 wt.%, 10 wt.% and 20 wt.% Nanohybrid CuO-Fe_3O_4/zeolite NCs were prepared and marked as 4-HCFZ NC, 10-HCFZ NC, and 20-HCFZ NC, respectively.

2.3. Characterization of x wt.% Nanohybrid CuO-Fe_3O_4/Zeolite NCs

The prepared samples powder X-ray diffraction (PXRD) patterns were obtained using a Shimadzu XRD-6000 instrument at a scan speed of 4°/min^{-1}

in a wide angle range of 2θ (5°-80°), current; 30 mA, Anode Material: Cu, and voltage ;30 kV. Transmission electron microscope (TEM) and field emission Scanning electron microscope (FESEM) analyses were conducted with a MODEL: JOEL JSM 7600F, the scanning electron microscope was set to 5 kV, and the H7100 transmission electron microscope was set to 120 kV, respectively. At 77 K, nitrogen adsorption-desorption isotherms were measured using a Quantachrome AS1 Win ™ (version 2.01) instrument. Fourier Transformed Infrared were collected in range 200-4000 Cm^{-1} using the series 100 PERKIN ELMER FTIR 1650 spectrophotometer. The lead and arsenic content of the solutions were determined using flame emission atomic absorption spectroscopy (AAS) (Thermo scientific, S series).

2.4. Preparation of Lead (II) and Arsenic (V) solution

As (V) and Pb (II) (1000 mg L^{-1}) are used to make two stock solutions. In one liter of deionized water, lead nitrate Pb $(NO_3)_2$ and sodium hydrogen arsenate $Na_2HAsO_4.7H_2O$ were dissolved separately. As a result, standard solutions for As (V) and Pb (II) with specific concentration ranges were prepared.

2.5. Batch adsorption experiments

Adsorption experiments were performed at room temperature and atmospheric pressure using a batch equilibration method, allowing the researchers to study the effect of various sorption process parameters (i.e. metal concentrations, adsorbent NCs amount, initial pH, and contact time). In brief, 0.05-0.20 g of the Nanohybrid CuO-Fe₃O₄/Zeolite NC adsorbent were separately added to 50 mL of toxic Pb (II) and As (V) solutions, with the initial toxic metal concentration (C_0) varying between 20 and 100 ppm (mg L^{-1}). Using 0.01 M HNO_3 and 0.01 M NaOH, the pH of the solution was previously adjusted from 2.0 to 6.0. The toxic metal solution's contents were stirred until they reached room temperature equilibrium. Aliquots of the system were taken at various time intervals and analyzed using atomic absorption spectroscopy. The following equation calculates the percentage removal of As (V) and Pb (II) [36]:

$$\text{Percentage removal} = \frac{(C_0 - C_e)}{C_0} \times 100 \qquad (1)$$

Where C_0 and C_e denote the initial lead and arsenic concentrations (mgL^{-1}) and equilibrium concentrations (mgL^{-1}), respectively. The following equation was used to calculate the adsorption capacity (q_e, mg g^{-1}) at equilibrium:

$$q_e = (C_0 - C_e)\frac{V}{w} \qquad (2)$$

where C_0 (mg/L) and C_e (mgL^{-1}) are the initial and equilibrium lead and arsenic concentrations, respectively; the volume of the water solution is denoted by V (L), and w is the weight of the solution (gram).

2.6. Adsorption isotherms

The adsorption equilibrium data for adsorption of the arsenic and lead ions on the Nanohybrid CuO-Fe₃O₄/zeolite NCs were investigated using Freundlich and Langmuir isotherm models that correspond to heterogeneous and homogeneous adsorbent surfaces, respectively.

2.7. Recovery experiment

To investigate the reusability of the prepared x wt% -HCFZ NCs as noval nanoadsorbents, Pb and As-adsorbed x wt% -HCFZ NCs were desorption and regeneration fourth times. In summary, the adsorbent was separated using filter papers following the adsorption process. The x wt% -HCFZ NCs as adsorbent with the adsorbed-toxic As or pb ions was then suspended for 30 mins in 20 mL (0.005 M) HNO₃ to desorb the toxic Pb (II) or As (V) ions. The nanohybrid CuO-Fe₃O₄/zeolite NCs were then separated using filter papers and centrifuge, washed three times with deionized water, and dried overnight at 80°C. Finally, the prepared HCFZ NCs samples were kept in a desiccator for further drying, and reuse.

3. RESULTS AND DISCUSSION

Various nanohybrid CuO-Fe₃O₄/zeolite NCs were prepared with x wt.% nanohybrid CuO-Fe₃O₄ into the zeolite. The nitrogen adsorption-desorption isotherms of 4-HCFZ NC, 10-HCFZ NC and 20-HCFZ NC are given in Fig. 1. From this figure, it can be seen that the nanohybrid CuO-Fe₃O₄/zeolite NCs exhibited IV isotherm adsorption behavior may be due to the existence of the zeolitic micropores [37]. Notably, all of the isotherms showed a steep increase when the relative pressure P/P₀ was greater than 0.2 (mostly monolayer) and a hysteresis loop when the relative pressure P/P₀ was between 0.2 and 1.0, which indicates the co-existence of a

Abdullah A. Alswat, Fares T. Al-shorifi, Shaimaa L. Ali

micro/mesoporous framework [18].

Fig. 1. BET of Zeolite, 4-HCFZ NC, 10-HCFZ NC and 20-HCFZ NC samples.

The BET surface area of the as prepared nanocomposites increased from 3.35 m^2/g to 9.227, 18.754, and 22.25 m^2/g for zeolite, 4-HCFZ NCs, 10-HCFZ NCs, and 20-HCFZ NCs, respectively. Table 1. The prepared x wt% -HCFZ NCs had a nearly six times higher surface area, indicating that the hybrid CuO-Fe$_3$O$_4$ NPs phases modified a porous layer on the surface and in the intracrystalline pores of the Zeolite structure. Furthermore, the formed Nanohybrid CuO-Fe$_3$O$_4$ NPs layer has a large surface area, which suggests a large number of functional groups and improve the adsorption process. However, as a consequence of filling these pores with Nanohybrid CuO- Fe$_3$O$_4$ NPs on the Zeolite, the Pore Volume decreased from 0.08 for the neat Zeolite to 0.066, 0.050, and 0.045 cc/g for 4-HCFZ NC, 10-HCFZ NC and 20-HCFZ NC samples, respectively as showed in Table 1. This decreasing in pore volume of x wt% -HCFZ NCs may be due filling the pore of neat Zeolite by nanohybrid CuO-Fe$_3$O$_4$ particles.

Form XRD results and according to the diffraction patterns of the neat Zeolite and x wt.% -HCFZ NCs depicted in Fig. 2, the peak profiles for the Fe$_3$O$_4$ and CuO NPs are in reference to Ref Codes 98-001-2051 and 98-005-3116, respectively.

The patterns suggest that the chemical zeolite structure has a typical face centered cubic (fcc) structure with reference to the Ref Cod 01-087-1619 data. It is observed that the hybrid CuO-Fe$_3$O$_4$ diffraction peaks that occurred in the peak profiles overlapped with the zeolite diffraction peaks. The particle sizes of nanohybrid Cu and Fe oxides in the prepared x wt.% -HCFZ NCs are determined by the Debye–Scherer equation:

$$D = \frac{k\lambda}{\beta \cos \theta} \tag{3}$$

where (λ)= 0.15418 nm is the X-ray wavelength, k= 0.94 is a coefficient, θ is the diffracting angle, and β is the sample's full-width half maximum. The average particle diameters were 7.32- 11.78 nm for the Nanohybrid CuO-Fe$_3$O$_4$ particles on the zeolites for all the HCFZ NC samples.

Fig. 2. XRD of 4, 10, and 20-HCFZ NC samples.

Fig. 3 depicts the FT-IR spectra of zeolite and 4, 10 and 20-HCFZ NCs samples.

The absorption in the region of 3627 cm^{-1} in the zeolite spectra corresponds to terminal silanol groups on the zeolite crystals' external surface. This peak, which overlaps with wide and strong peaks, corresponds to O-H stretching in the spectral range 3100-3500 cm^{-1}.

The O-H bending vibration is represented by the peak at 1673 cm^{-1}. The absorption that can be seen in range of 900 to 1200 cm^{-1} is attributed to stretching and bending modes of Al–O or Si–O in a zeolite framework.

Table 1. BET pore volume and surface area of x wt% -HCFZ NCs.

	Unit	**Neat zeolite**	**4-HCFZ NC**	**10-HCFZ NC**	**20-HCFZ NC**
Surface Area	m^2/g	3.35	9.227	18.754	22.25
Pore Volume	cc/g	0.08	0.066	0.05	0.045

4

Fig. 3. FT-IR of Neat-Zeolite and 4-HCFZ NCs, 10-HCFZ NCs and 20-HCFZ NCs.

For example, the bands around 1120 cm^{-1} are associated with the symmetric and asymmetric stretching modes of internal tetrahedra, while the bands around 1017 cm^{-1} are related to the symmetric and asymmetric stretching modes of external linkages.

Because of the presence of CuO NPs and Fe_3O_4 NPs as Nanohybrid metal oxides on the zeolite, the spectra of x wt% -HCFZ NCs differ significantly from the spectra of zeolite in the spectral regions 300 to 700 cm^{-1}. Peaks in the x wt% -HCFZ NCs spectra in the spectral regions 674 and 661 cm^{-1}, 585 cm^{-1}, 543, and 347 cm^{-1} [38] correspond to Fe^{2+}–O–Fe^{3+}, Fe^{3+}–O, and Fe^{2+}, while the zeolite spectra did not show those peaks.

It is worth noting that after the ion-exchange process, no band appears around 1380–1390 cm^{-1}, which is assigned to the $CuNO_3$ compound as nitrate stretching vibrations (1380 cm^{-1}), confirming that the catalyst is converted to CuO [39]. In point of fact, when comparing the FT-IR spectrum of a sample containing copper oxide nanoparticles to the pure

Zeolite spectrum, we can conclude that there is a small decrease in peak broadening, intensity, and shifting of the peak from 357 cm^{-1} to 353 cm^{-1} for the presence of CuO NPs, which can be attributed to the Cu–O bond of x wt% -HCFZ NCs samples [40]. Generally, maybe say that the small blue shift in peak positions and the decrease in peak intensities in FT-IR spectrum figure demonstrated that Nanohybrid CuO-Fe_3O_4 particles precipitated in the crystal zeolite structure and/or in the porous zeolite system; these results are consistent with XRD, TEM, and FESEM.

The chemical elements are identified by EDX analysis. Fig.4 and Table 2 represent all elements that were expected to be in the chemical composition of the selected 20-HCFZ NC sample. Peaks at 0.55 keV, 1.05 keV, 1.50 keV, and 1.75 keV correspond to the binding energies of O, Na, Al, and Si in the chemical zeolite structure, respectively. Furthermore, in the EDX spectra of 20-HCFZ NCs, the peaks of the binding energies of Fe were around 6.40 keV and 7.05 keV, while the peaks the binding energies of Cu were at 8.05 and 9.00 keV. These peaks indicating the existence of both of Fe and Cu as Nanohybrid oxides in the prepared HCFZ NC catalysts [41]

The TEM images in Fig.5 (a and b) showed the typical structure and smooth surface of the neat zeolite, which has a cubic shape, whereas the surface of x wt.% -HCFZ NC seems to have nanospheres and some different granular shapes, which confirms presence of CuO and Fe_3O_4 NPs as Nanohybrid Cu and Fe oxides in the prepared-HCFZ NC samples. Similarly, the cubic zeolite shape did not change when Nanohybrid CuO-Fe_3O_4 NPs were formed on it, confirming the results of the BET and XRD analyses.

The different granular shapes due to mixing of CuO and Fe_3O_4 together may be due different

Table 2. EDX of 20-HCFZ NC sample.

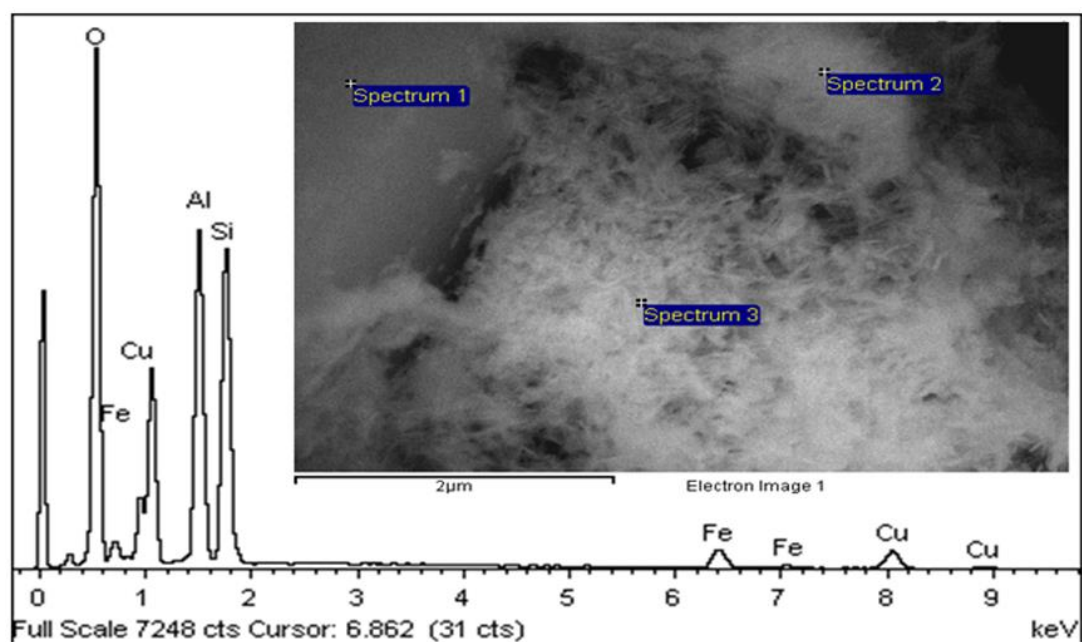| Spectrum	In stats.	O	Al	Si	Fe	Cu	Total
Spectrum 1	Yes	59.11	14.75	16.64	3.50	6.00	100.00
Spectrum 2	Yes	40.60	12.32	11.65	10.60	24.83	100.00
Spectrum 3	Yes	44.03	10.78	10.55	1.88	32.77	100.00
Mean		47.91	12.62	12.95	5.33	21.20	100.00
Std. deviation		9.85	2.00	3.25	4.64	13.75	
Max.		59.11	14.75	16.64	10.60	32.77	
Min.		40.60	10.78	10.55	1.88	6.00	

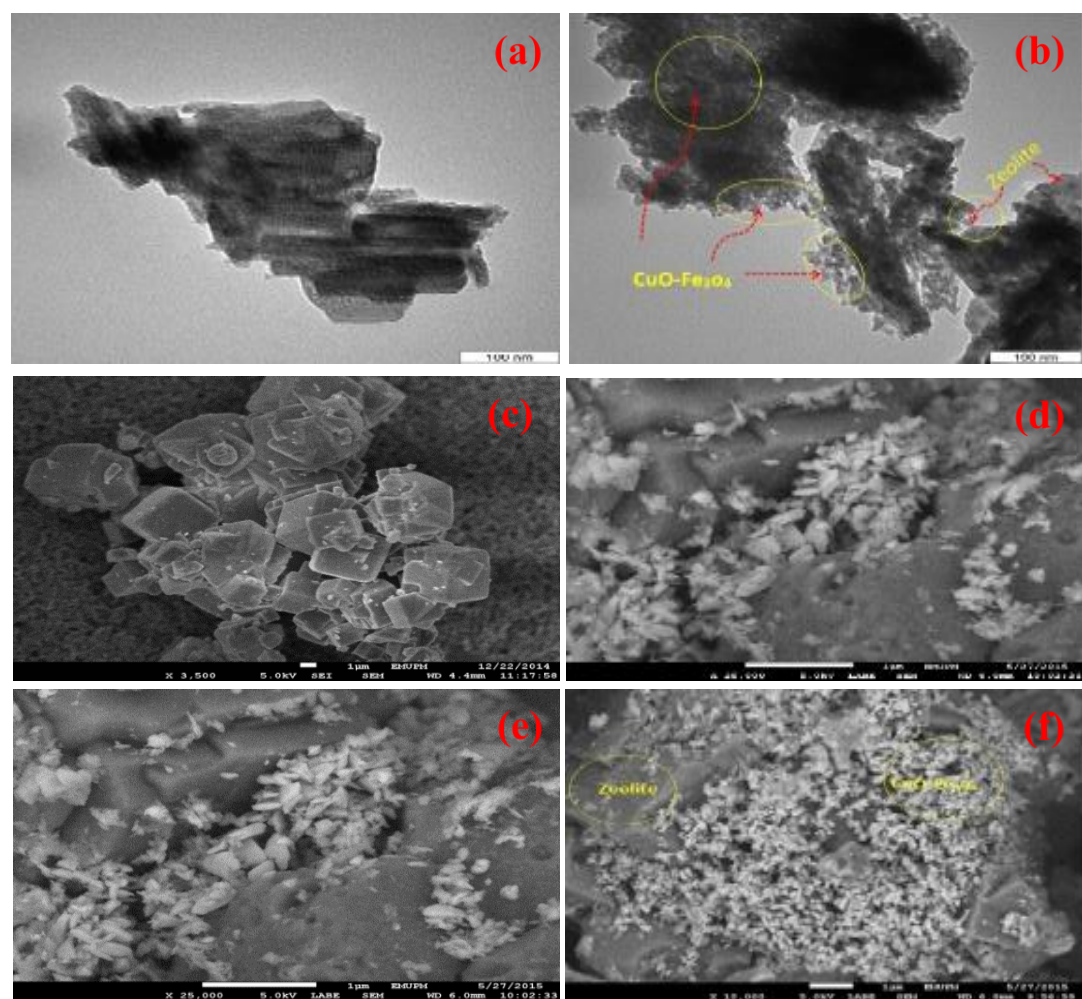**Fig. 4.** EDX of 20-HCFZ NC sample.

Fig. 5. TEM images of a) neat Zeolite b) 20-HCFZ NC sample and FESEM images of c) neat Zeolite, d) 4-HCFZ NC, e) 10-HCFZ NC, f) 20-HCFZ NC samples.

oxidation state of iron metal in Fe_3O_4 compound (Fe^{3+}) and Fe^{2+}) which led to form of defects in crystal lattice of Nanohybrid metal oxides. It can be clearly seen that the Nanohybrid Cu and Fe oxide NPs immobilized on the neat Zeolite surface as Nanohybrid CuO-Fe_3O_4 with average diameter 8.95-11.44 nm.

The obtained Nanosizes of Nanohybrid Cu and Fe oxides are in agreement with average crystallite sizes calculated from XRD by the Scherer equation. FESEM images Fig. 5 (c, d, e, and f), confirmed that the neat-zeolite has a cubic structure and the CuO and Fe_3O_4 NPs formed on the zeolite surfaces as Nanohybrid Cu and Fe oxides. It can be clearly seen that the Nanohybrid Cu and Fe oxide NPs distributed on the external surface of zeolite, with different shapes (nano spherical, nanocylinder). The Presence different shapes on the Zeolite surface may be due to presence some defects on lattices of both Cu and Fe in result of mixing them up with some.

3.1. Adsorption efficiency

Under the optimum adsorption parameters (pH= 4, time= 30 min, dosage= 0.15 g, initial concentration 100 ppm) the removal of As and Pb ions by x wt% Nanohybrid CuO-Fe_3O_4/Zeolite NC adsorbent was performed. From Fig. 6, the 10-HCFZ NC showed the highest removal efficiency of harmful metals from water compared with the pure Zeolite, 4-HCFZ NC and 20-HCFZ NC samples with the percentage of removal (97.9, 60.0, 81.2, and 87.5%) for Pb ions and (93.5, 54.0, 79.8, and 82.3 %) for As ions, respectively. The higher removal efficiency of 10-HCFZ NCs for As and Pb ions can be related to the joint influence of a large specific area, the availability of further active sites, and the high porosity.
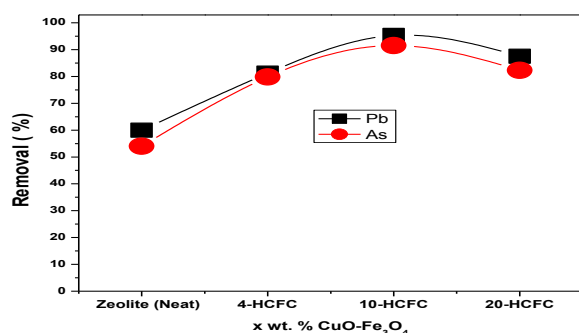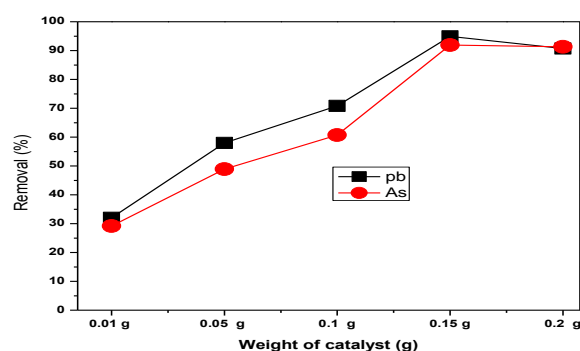

Fig. 6. As (V) and Pb (II) removal percentages by time 30 min, and dose 0.15 g. pure Zeolite and 4, 10, and 20-HCFZ NCs; concentration 100 mgL^{-1}, 50 mL solution, pH 4, contact

In regards to the influence of functional groups incorporated to the Zeolite's surface by Fe_3O_4 and CuO, there are two key parameters that can clarify the mechanism of Pb and As removal by the prepared catalysts: metal ions proceeded through the crystal lattice channels or through the pores of the 10-HCFZ NCs. The ion exchange reaction between the protons on the metal ions and the surface of NCs is another important factor.

3.2. Effect of the catalyst weight

Fig. 7 shows the results of the HCFZ NCs adsorbent dosage on the efficiency of arsenic (V) and Pb (II) removal. Initially, adsorption of arsenic and lead cations by 10-HCFZ NC increased from 32.0 to 97.9% and from 29.2 to 93.9% respectively. Then, a significantly decrease in adsorption efficiency for arsenic and lead cations below the previous mentioned values.

The adsorption capacity was initially increased as a result of the variety of adsorption sites besides the larger surface area incorporated by increasing the frequency of adsorbent particles [42]. However, the aggregation of high adsorbent dose from 0.15 to 0.20 g for both metals as expected decreased the percentage of adsorption, resulting in a decrease in adsorbent surface area, or it could be due to either insufficient metal ions in solution compared to available binding sites or interference between higher adsorbed dose and binding sites [43].


Fig. 7. Effect of adsorbent dosage on As (V) and Pb (II) removal percentages by 10-HCFZ NCs; concentration 100 mgL^{-1}, 50 mL solution, contact time 30 min, and pH 4.

3.3. Effect of the metallic pollutant concentration

Arsenic and lead adsorption was tested at initial concentrations varying from 20 to 100 mgL^{-1}. Fig. 8 presents that increasing the initial metal

concentration reduces the percentage of removal from 99.8 to 97.7% for lead ions and from 99.0 to 93.7% for arsenic ions. This decrease could be attributed to the HCFZ NC adsorbent's limited number of active sites, which become more saturated as the metal ion concentration increases. In contrast, increasing the initial As (V) and Pb (II) concentrations resulted in an increase in adsorption capacity across the concentration range studied. Higher concentrations of As (V) and Pb (II) resulted in the adsorption process continuing because the active sites of the 10-HCFZ NC adsorbent were surrounded by much more metal ions, resulting in a higher amount of As (V) and Pb (II) adsorbed from the water solution. As a result, as the initial metal ion concentrations increase, so do the values of q_e (C_0).
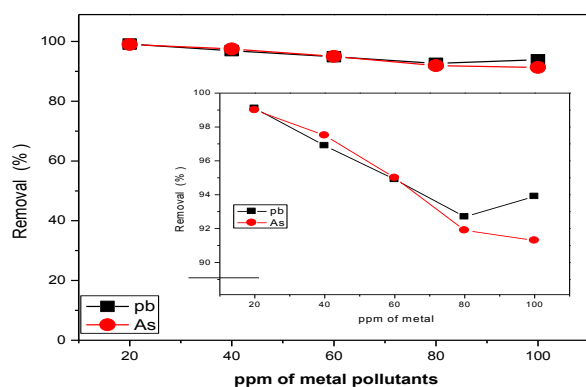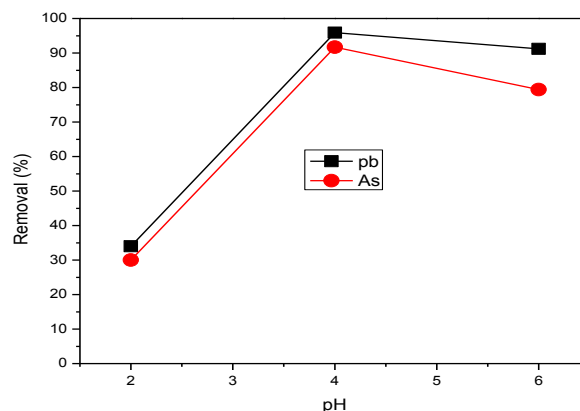

Fig. 8. Effect of initial concentrations of As (V) and Pb (II) on removal percentages by 10-HCFZ NCs; 50 mL solution, contact time 30 min, pH 4, and dose 0.15 g.

The adsorption process in which metal ions proceeded through the pores or through channels of the crystal lattice of the 10-HCFZ NC could explain this. The ion exchange reaction between protons on the surface of 10-HCFZ NCs and metal ions is another important factor [44].

3.4. Effect of the solution pH

The pH of the solution influences metal adsorption on the adsorbent as chemical precipitation of metal hydroxide occurs at higher pH values [45]. Therefore, the effect of pH on the adsorption of As and Pb ions on 10-HCFZ NC sample was studied over a pH range of 2.0 to 6.0, as shown in Fig. 9. The involvement of acidic medium (H^+) in the solution competes with As (V) and Pb (II) for active sites on the adsorbents

surface, resulting in lower adsorption [6]. At pH 4, the maximum removal efficiency for Pb (II) was 97.9% and 93.7% for As (V).

Fig. 9. Effect of pH solution of As (V) and Pb (II) on removal percentages by 10-HCFZ NCs; 50 mL solution, contact time 30 min, and dose 0.15 g, concentration 100 mgL^{-1}.

The decreasing in removal percent of metallic pollutants at pH= 6.0 is may be due to increasing hydroxide anions that form an ionic sphere around the pb and As cations in result of the different charges which leaded electrostatically attractions between hydroxide anions and metallic pollutant cations and thus the adsorption on the catalyst surface decreased. On the other hand, sodium ions in pollutant solution also will increase, so we can say that Na ions competed with pollutant metal ions on the adsorption on active sites of catalyst surface.
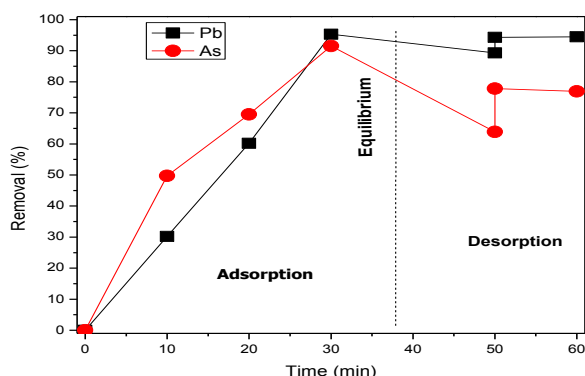
3.5. Effect of contact time

The level of arsenic and lead removal by the 10-HCFZ NC sample was discovered to increase with the contact time, reaching a maximum after 30 minutes as shown in Fig. 10.
Following that, it decreases as contact time increases, possibly due to a desorption process. As the of available adsorption sites decreased, the amount of As (V) and Pb (II) adsorbed increased with increasing contact time. Large numbers of vacant surface sites are available during the initial adsorption stage, but after a period of time, the vacant surface sites are almost saturated with As (V) and Pb (II) and are difficult to occupy due to repulsive forces between the solute molecules on the solid and the bulk phases [46]. As a consequence, the adsorption rate approach slows down in the

8

subsequent period.

Fig. 10. Effect of contact time on removal percentages of As (V) and Pb (II) by 10-HCFZ NCs; 50 mL solution, pH 4, dose 0.15 g, and concentration 100 mgL^{-1}.

3.6. Adsorption isotherms

The adsorption equilibrium data were fitted using the Langmuir and Freundlich models in this study to investigate the distribution of arsenic (V) and lead Pb (II) between the solid phases (the prepared NCs) and the bulk solution of As and Pb at equilibrium.

The Langmuir model is an empirical model that assumes adsorption occurs on the adsorbent's surface at uniform energy sites. The Freundlich model, on the other hand, assumes that multilayer adsorption occurs due to the diversity of adsorption sites.

Langmuir isotherms: The Langmuir model explains the amount of arsenic (V) and lead Pb (II) adsorbed and has the following linear equation:

$$\frac{C_e}{q_e} = \frac{1}{bq_m} + \frac{C_e}{q_m} \tag{4}$$

where q_e (mgg^{-1}) is the amount adsorbed at equilibrium, C_e (mgL^{-1}) is the concentration at equilibrium of arsenic (V) and lead Pb (II) in the solution, b, and q_m (mgg^{-1}) are the Langmuir constants related to adsorption energy and maximum monolayer capacity (adsorption efficiency), respectively [33].

Fig. 11 depicts the plot C_e/q_e versus C_e, and Table 3 shows the values q_m and b. The maximum monolayer capacity q_m by the 10-HCFZ NC sample for lead (56.02 mgg^{-1}) is significantly greater than q_m of Arsenic (45.66 mgg^{-1}), which is consistent with the results obtained above. The separation factor (R_L) was determined to assure the adsorption process's
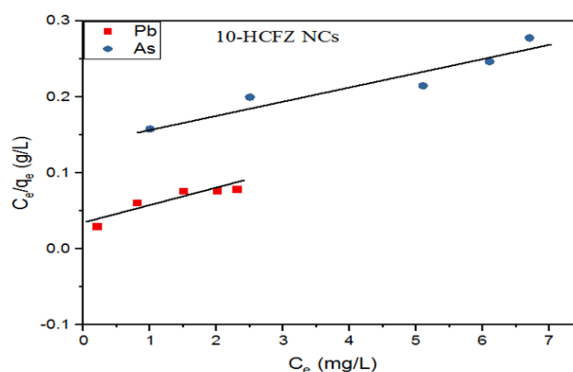
suitability.

$$R_L = \frac{1}{1+bC_0} \tag{5}$$

Where C_0 is the highest initial As (V) and Pb (II) concentration (mgL^{-1}) and b (Lmg^{-1}) is the Langmuir constant. The R_L values suggest that arsenic (V) and lead Pb (II) adsorption onto the prepared NCs is a favorable process.
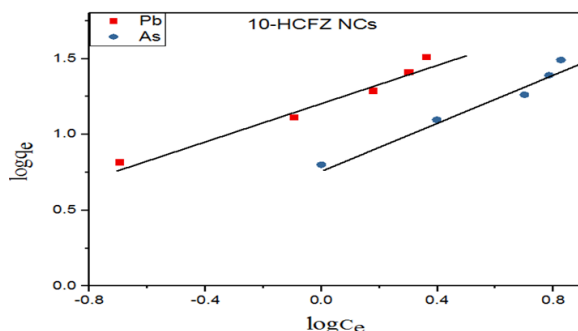
Freundlich isotherm: The Freundlich model is represented by this equation:

$$\ln q_e = \ln K_f + \frac{1}{n}\ln C_e \tag{6}$$

Fig. 11. Langmuir isotherm plot for adsorption of lead arsenic (V) and Pb (II) by 10-HCFZ NC sample.

where n is the Freundlich constant based on the adsorption intensity, calculated from the slope, and K_f (mg.g^{-1}) is the Freundlich constant based on the adsorption capacity of NCs catalysts, calculated from the intercept, where 1/n (gL^{-1}) indicates how favorable the adsorption process is [16, 36, 47–51]. Fig. 12 illustrates the plot of $\ln q_e$ versus $\ln C_e$.

Fig. 12. Freundlich isotherm plot for adsorption of lead Pb (II) and arsenic (V) by 10-HCFZ NC sample.

Table 3 shows the values of n and K_f derived from the slopes and intercepts. According to the results, the R2 values of the Langmuir isotherm model are greater than those of the Freundlich isotherm model,

Table 3. The adsorption isotherm model parameters of arsenic (V) and lead Pb (II) adsorption by 10-HCFZ NCs.

Adsorbent 10-HCFZ NCs	Langmuir isotherm			Freundlich isotherm		
	b (L mg^{-1})	q_m (mg g^{-1})	R^2	K_f $\left((mg\ g^{-1})/(mg\ mL^{-1})^{1/n}\right)$	n	R^2
Lead (Pb)	0.525	56.02	0.997	3.4	1.6	0.978
Arsenic (As)	0.168	45.66	0.994	2.2	1.29	0.959

suggesting that the experimental data fit better with the Langmuir isotherm model. The prepared 10-HCFZ sample was clearly useful and applicable materials for efficient arsenic and lead removal from aqua solutions.

4. CONCLUSIONS

Copper oxide (CuO)/zeolites and ferric oxide (Fe$_3$O$_4$)/zeolites have been studied as sorption materials for environmentally unfriendly metals removal from aqueous systems. However, these studies have not focused on preparing a nanocomposite made of hybrid CuO-Fe$_3$O$_4$, and zeolite (Nanohybrid CuO-Fe$_3$O$_4$ /Zeolite NCs) with superior removal capacity for the toxic metallic pollutants. In our current study, we tested the extent to which the nanohybrid CuO-Fe$_3$O$_4$/Zeolite NCs could capture the toxic lead and arsenic cations from contaminated aqueous solutions. From the obtained experimental results, the 10-HCFZ NC sample showed the highest removal efficiency (97.9%) for Pb cations and (93.5%) for As cations within 30 minutes (100 ppm). These findings extend the previous studies, confirming that the Nanohybrid CuO-Fe$_3$O$_4$/Zeolite NCs tend to be more effective and superior. Most notably, based on the authors' knowledge this is the first study to synthesize the nanohybrid CuO-Fe$_3$O$_4$/Zeolite NC catalysts with promising adsorption capacity for environmentally unfriendly metallic pollutants.

REFERENCES

[1] Abdullah, N. H.; Shameli, K.; Abdullah, E. C.; Abdullah, L. C. Solid Matrices for Fabrication of Magnetic Iron Oxide Nanocomposites: Synthesis, Properties, and Application for the Adsorption of Heavy Metal Ions and Dyes. Compos. Part B Eng. 2019, 162, 538–568.

[2] Al-Hossainy, A. F.; Abdelaal, R. M.; El Sayed, W. N. Novel Synthesis, Structure Characterization, DFT and Investigation of the Optical Properties of Cyanine Dye/Zinc Oxide [4-CHMQI/ZnO] C Nanocomposite Thin Film. J. Mol. Struct. 2021, 1224, 128989.

[3] Vorozhtsov, S.; Zhukov, I.; Vorozhtsov, A.; Zhukov, A.; Eskin, D.; Kvetinskaya, A. Synthesis of Micro-and Nanoparticles of Metal Oxides and Their Application for Reinforcement of Al-Based Alloys. Adv. Mater. Sci. Eng. 2015, vol. 2015, 1-6. https://doi.org/10.1155/2015/718207

[4] Dizaj, S. M.; Lotfipour, F.; Barzegar-Jalali, M.; Zarrintan, M. H.; Adibkia, K. Antimicrobial Activity of the Metals and Metal Oxide Nanoparticles. Mater. Sci. Eng. C 2014, 44, 278–284.

[5] Mannaa, M. A.; Qasim, K. F.; Alshorifi, F. T.; El-Bahy, S. M.; Salama, R. S. Role of NiO Nanoparticles in Enhancing Structure Properties of TiO$_2$ and Its Applications in Photodegradation and Hydrogen Evolution. ACS omega 2021, 6 (45), 30386–30400.

[6] El-Yazeed, W. S. A.; El-Hakam, S. A.; Salama, R. S.; Ibrahim, A. A.; Ahmed, A. I. Ag-PMA Supported on MCM-41: Surface Acidity and Catalytic Activity. J. Sol-Gel Sci. Technol. 2022, 1–13. DOI:10.1007/s10971-022-05755-7

[7] Altass, H. M.; Morad, M.; Khder, A. E.-R. S.; Mannaa, M. A.; Jassas, R. S.; Alsimaree, A. A.; Ahmed, S. A.; Salama, R. S. Enhanced Catalytic Activity for CO Oxidation by Highly Active Pd Nanoparticles Supported on Reduced Graphene Oxide/Copper Metal Organic Framework. J. Taiwan Inst. Chem. Eng. 2021, 128, 194–208.

[8] Alshorifi, F. T.; Alswat, A. A.; Mannaa, M.

A.; Alotaibi, M. T.; El-Bahy, S. M.; Salama, R. S. Facile and Green Synthesis of Silver Quantum Dots Immobilized onto a Polymeric CTS–PEO Blend for the Photocatalytic Degradation of p-Nitrophenol. ACS Omega 2021, 6, 30432–30441.

[9]   Altass, H. M.; Khder, A. S.; Ahmed, S. A.; Morad, M.; Alsabei, A. A.; Jassas, R. S.; Althagafy, K.; Ahmed, A. I.; Salama, R. S. Highly Efficient, Recyclable Cerium-Phosphate Solid Acid Catalysts for the Synthesis of Tetrahydrocarbazole Derivatives by Borsche–Drechsel Cyclization. React. Kinet. Mech. Catal. 2021, 134, 143–161.

[10]   Salama, R. S.; Mannaa, M. A.; Altass, H. M.; Ibrahim, A. A.; Khder, A. E. R. S. Palladium Supported on Mixed-Metal-Organic Framework (Co-Mn-MOF-74) for Efficient Catalytic Oxidation of CO. RSC Adv. 2021, 11 (8), 4318–4326. https://doi.org/10.1039/d0ra09970h.

[11]   El-Hakam, S. A.; ALShorifi, F. T.; Salama, R. S.; Gamal, S.; El-Yazeed, W. S. A.; Ibrahim, A. A.; Ahmed, A. I. Application of Nanostructured Mesoporous Silica/Bismuth Vanadate Composite Catalysts for the Degradation of Methylene Blue and Brilliant Green. J. Mater. Res. Technol. 2022, 18, 1963–1976.

[12]   Altass, H. M.; Morad, M.; Khder, A. S.; Raafat, M.; Alsantali, R. I.; Khder, M. A.; Salama, R. S.; Malik, M. S.; Moussa, Z.; Abourehab, M. A. S. Exploitation the Unique Acidity of Novel Cerium-Tungstate Catalysts in the Preparation of Indole Derivatives under Eco-Friendly Acid Catalyzed Fischer Indole Reaction Protocol. Arab. J. Chem. 2022, 15 (3), 103670.

[13]   El-Hakam, S. A.; Samra, S. E.; El-Dafrawy, S. M.; Ibrahim, A. A.; Salama, R. S. Surface Acidity and Catalytic Activity of Sulfated Titania Supported on Mesoporous MCM-41. Int. J. Mod. Chem. Int. J. Mod. Chem. J. homepage www.ModernScientificPress.com/Journals /IJMChem.aspx 2013, 5 (1), 55–70.

[14]   Salama, R. S.; El-Hakam, S. A.; Samra, S. E.; El-Dafrawy Sh, M.; Ahmed, A. I. Cu-BDC as a Novel and Efficient Catalyst for the Synthesis of 3, 4-Dihydropyrimidin-2 (1H)-Ones and Aryl-14H-Dibenzo [a, j] Xanthenes under Conventional Heating. Intern. J. Nano Mater. Scien 2018, 7 (1), 31–42.

[15]   Salama, R. S.; Hassan, S. M.; Ahmed, A. I.; El-Yazeed, W. S. A.; Mannaa, M. A. The Role of PMA in Enhancing the Surface Acidity and Catalytic Activity of a Bimetallic Cr–Mg-MOF and Its Applications for Synthesis of Coumarin and Dihydropyrimidinone Derivatives. RSC Adv. 2020, 10 (36), 21115–21128.

[16]   Mannaa, M. A.; Altass, H. M.; Salama, R. S. MCM-41 Grafted with Citric Acid: The Role of Carboxylic Groups in Enhancing the Synthesis of Xanthenes and Removal of Heavy Metal Ions. Environ. Nanotechnology, Monit. Manag. 2021, 15, 100410.

[17]   Salama, R. S.; El-Bahy, S. M.; Mannaa, M. A. Sulfamic Acid Supported on Mesoporous MCM-41 as a Novel, Efficient and Reusable Heterogenous Solid Acid Catalyst for Synthesis of Xanthene, Dihydropyrimidinone and Coumarin Derivatives. Colloids Surfaces A Physicochem. Eng. Asp. 2021, 628 (June), 127261. https://doi.org/10.1016/j.colsurfa.2021.12 7261.

[18]   Tao, H.; Yang, H.; Liu, X.; Ren, J.; Wang, Y.; Lu, G. Highly Stable Hierarchical ZSM-5 Zeolite with Intra-and Inter-Crystalline Porous Structures. Chem. Eng. J. 2013, 225, 686–694.

[19]   Alkordi, M. H.; Liu, Y.; Larsen, R. W.; Eubank, J. F.; Eddaoudi, M. Zeolite-like Metal− Organic Frameworks as Platforms for Applications: On Metalloporphyrin-Based Catalysts. J. Am. Chem. Soc. 2008, 130 (38), 12639–12641.

[20]   Sarkar, S.; Guibal, E.; Quignard, F.; SenGupta, A. K. Polymer-Supported Metals and Metal Oxide Nanoparticles: Synthesis, Characterization, and Applications. J. Nanoparticle Res. 2012, 14 (2), 1–24.

[21]   Sani, H. A.; Ahmad, M. B.; Saleh, T. A. Synthesis of Zinc Oxide/Talc Nanocomposite for Enhanced Lead Adsorption from Aqueous Solutions. RSC

Adv. 2016, 6 (110), 108819–108827.

[22] Hu, G.; Yang, J.; Duan, X.; Farnood, R.; Yang, C.; Yang, J.; Liu, W.; Liu, Q. Recent Developments and Challenges in Zeolite-Based Composite Photocatalysts for Environmental Applications. Chem. Eng. J. 2021, 417, 129209.

[23] Lee, J. K.; Turrina, A.; Zhu, L.; Seo, S.; Zhang, D.; Cox, P. A.; Wright, P. A.; Qiu, S.; Hong, S. B. An Aluminophosphate Molecular Sieve with 36 Crystallographically Distinct Tetrahedral Sites. Angew. Chemie 2014, 126 (29), 7610–7613.

[24] Esmaeili, S.; Hemami, M.-R.; Goheen, J. R. Human Dimensions of Wildlife Conservation in Iran: Assessment of Human-Wildlife Conflict in Restoring a Wide-Ranging Endangered Species. PLoS One 2019, 14 (8), e0220702.

[25] Liu, C.; Pidko, E. A.; Hensen, E. J. M. Origin of Enhanced Brønsted Acidity of NiF-Modified Synthetic Mica–Montmorillonite Clay. Catal. Sci. Technol. 2018, 8 (1), 244–251.

[26] Alswat, A. A.; Ahmad, M. Bin; Saleh, T. A. Preparation and Characterization of Zeolite\zinc Oxide-Copper Oxide Nanocomposite: Antibacterial Activities. Colloid Interface Sci. Commun. 2017, 16, 19–24.

[27] Tedla, H.; Díaz, I.; Kebede, T.; Taddesse, A. M. Synthesis, Characterization and Photocatalytic Activity of Zeolite Supported $ZnO/Fe_2O_3/MnO_2$ Nanocomposites. J. Environ. Chem. Eng. 2015, 3 (3), 1586–1591.

[28] Alswat, A. A.; Ahmad, M. Bin; Al-Hada, N. M.; Kamari, H. M.; Hussein, M. Z. Bin; Ibrahim, N. A. Preparation of Zeolite/Zinc Oxide Nanocomposites for Toxic Metals Removal from Water. Results Phys. 2017, 7, 723–731.

[29] Alswat, A. A.; Ahmad, M. Bin; Saleh, T. A. Zeolite Modified with Copper Oxide and Iron Oxide for Lead and Arsenic Adsorption from Aqueous Solutions. J. Water Supply Res. Technol. 2016, 65 (6), 465–479.

[30] Shokrolahi, S.; Farhadian, M.; Davari, N. Degradation of Enrofloxacin Antibiotic in Contaminated Water by ZnO/Fe$_2$O$_3$/Zeolite Nanophotocatalyst. J. Appl. Res. Water Wastewater 2019, 6 (2), 150–155.

[31] Wang, Q.; Yang, Z. Industrial Water Pollution, Water Environment Treatment, and Health Risks in China. Environ. Pollut. 2016, 218, 358–365.

[32] Zeitoun, M. M.; Mehana, E. E. Impact of Water Pollution with Heavy Metals on Fish Health: Overview and Updates. Glob. Vet. 2014, 12 (2), 219–231.

[33] Siraj, K.; Kitte, S. A. Analysis of Copper, Zinc and Lead Using Atomic Absorption Spectrophotometer in Ground Water of Jimma Town of Southwestern Ethiopia. Int. J. Chem. Anal. Sci. 2013, 4 (4), 201–204.

[34] Limón-Pacheco, J. H.; Jiménez-Córdova, M. I.; Cárdenas-González, M.; Retana, I. M. S.; Gonsebatt, M. E.; Del Razo, L. M. Potential Co-Exposure to Arsenic and Fluoride and Biomonitoring Equivalents for Mexican Children. Ann. Glob. Heal. 2018, 84 (2), 257.

[35] Bhattacharya, S.; Sharma, P.; Mitra, S.; Mallick, I.; Ghosh, A. Arsenic Uptake and Bioaccumulation in Plants: A Review on Remediation and Socio-Economic Perspective in Southeast Asia. Environ. Nanotechnology, Monit. Manag. 2021, 15, 100430.

[36] Salama, R. S.; El-Hakama, S. A.; Samraa, S. E.; El-Dafrawya, S. M.; Ahmeda, A. I. Adsorption, Equilibrium and Kinetic Studies on the Removal of Methyl Orange Dye from Aqueous Solution by Using of Copper Metal Organic Framework (Cu-BDC). Int. J. Mod. Chem 2018, 10 (2), 195–207.

[37] Sing, K. S. W. Reporting Physisorption Data for Gas/Solid Systems with Special Reference to the Determination of Surface Area and Porosity (Recommendations 1984). Pure Appl. Chem. 1985, 57 (4), 603–619.

[38] Jahangirian, H.; Ismail, M. H. S.; Haron, M. J.; Rafiee-Moghaddam, R.; Shameli, K.; Hosseini, S.; Kalantari, K.; Khandanlou, R.; Gharibshahi, E.; Soltaninejad, S. Synthesis and Characterization of Zeolite/Fe$_3$O$_4$ Nanocomposite by Green Quick

12

Precipitation Method. Dig J Nanomater Biostruct 2013, 8 (4), 1405–1413.

[39]   El-Dafrawy, S. M.; Salama, R. S.; El-Hakam, S. A.; Samra, S. E. Bimetal-Organic Frameworks (Cux-Cr100-x-MOF) as a Stable and Efficient Catalyst for Synthesis of 3, 4-Dihydropyrimidin-2-One and 14-Phenyl-14H-Dibenzo [a, j] Xanthene. J. Mater. Res. Technol. 2020, 9 (2), 1998–2008. https://doi.org/10.1016/j.jmrt.2019.12.032.

[40]   Lihitkar, P. B.; Violet, S.; Shirolkar, M.; Singh, J.; Srivastava, O. N.; Naik, R. H.; Kulkarni, S. K. Confinement of Zinc Oxide Nanoparticles in Ordered Mesoporous Silica MCM-41. Mater. Chem. Phys. 2012, 133 (2–3), 850–856.

[41]   Chang, Y.-P.; Ren, C.-L.; Qu, J.-C.; Chen, X.-G. Preparation and Characterization of Fe_3O_4/Graphene Nanocomposite and Investigation of Its Adsorption Performance for Aniline and p-Chloroaniline. Appl. Surf. Sci. 2012, 261, 504–509.

[42]   Hao, Y.-M.; Man, C.; Hu, Z.-B. Effective Removal of Cu (II) Ions from Aqueous Solution by Amino-Functionalized Magnetic Nanoparticles. J. Hazard. Mater. 2010, 184 (1–3), 392–399.

[43]   Li, Z.; Wang, L.; Wu, J.; Xu, Y.; Wang, F.; Tang, X.; Xu, J.; Ok, Y. S.; Meng, J.; Liu, X. Zeolite-Supported Nanoscale Zero-Valent Iron for Immobilization of Cadmium, Lead, and Arsenic in Farmland Soils: Encapsulation Mechanisms and Indigenous Microbial Responses. Environ. Pollut. 2020, 260, 114098.

[44]   Kong, S.; Wang, Y.; Zhan, H.; Yuan, S.; Yu, M.; Liu, M. Adsorption/Oxidation of Arsenic in Groundwater by Nanoscale Fe-Mn Binary Oxides Loaded on Zeolite. Water Environ. Res. 2014, 86 (2), 147–155.

[45]   Salem Attia, T. M.; Hu, X. L.; Yin, D. Q. Synthesised Magnetic Nanoparticles Coated Zeolite (MNCZ) for the Removal of Arsenic (As) from Aqueous Solution. J. Exp. Nanosci. 2014, 9 (6), 551–560.

[46]   Ibrahim, A. A.; Ali, S. L.; Adly, M. S.; El-Hakam, S. A.; Samra, S. E.; Ahmed, A. I. Green Construction of Eco-Friendly Phosphotungstic Acid Sr-MOF Catalysts for Crystal Violet Removal and Synthesis of Coumarin and Xanthene Compounds. RSC Adv. 2021, 11 (59), 37276–37289.

[47]   Ibrahim, A. A.; Salama, R. S.; El-Hakam, S. A.; Khder, A. S.; Ahmed, A. I. Synthesis of 12-Tungestophosphoric Acid Supported on Zr/MCM-41 Composite with Excellent Heterogeneous Catalyst and Promising Adsorbent of Methylene Blue. Colloids Surfaces A Physicochem. Eng. Asp. 2021, 631, 127753.

[48]   El-Hakam, S. A.; Ibrahim, A. A.; Elatwy, L. A.; El-Yazeed, W. S. A.; Salama, R. S.; El-Reash, Y. G. A.; Ahmed, A. I. Greener Route for the Removal of Toxic Heavy Metals and Synthesis of 14-Aryl-14H Dibenzo[a,j] Xanthene Using a Novel and Efficient Ag-Mg Bimetallic MOF as a Recyclable Heterogeneous Nanocatalyst. J. Taiwan Inst. Chem. Eng. 2021, 122, 176–189. https://doi.org/10.1016/j.jtice.2021.04.036.

[49]   Salama, R. S.; El-Sayed, E. S. M.; El-Bahy, S. M.; Awad, F. S. Silver Nanoparticles Supported on UiO-66 (Zr): As an Efficient and Recyclable Heterogeneous Catalyst and Efficient Adsorbent for Removal of Indigo Carmine. Colloids Surfaces A Physicochem. Eng. Asp. 2021, 626 (May), 127089. https://doi.org/10.1016/j.colsurfa.2021.12 7089.

[50]   El-Hakam, S. A.; Samra, S. E.; El-Dafrawy, S. M.; Ibrahim, A. A.; Salama, R. S.; Ahmed, A. I. Synthesis of Sulfamic Acid Supported on Cr-MIL-101 as a Heterogeneous Acid Catalyst and Efficient Adsorbent for Methyl Orange Dye. RSC Adv. 2018, 8 (37), 20517–20533. https://doi.org/10.1039/c8ra02941e.

[51]   Ibrahim, A. A.; Salama, R. S.; El-Hakam, S. A.; Khder, A. S.; Ahmed, A. I. Synthesis of Sulfated Zirconium Supported MCM-41 Composite with High-Rate Adsorption of Methylene Blue and Excellent Heterogeneous Catalyst. Colloids Surfaces A Physicochem. Eng. Asp. 2021, 616 (February), 126361. https://doi.org/10.1016/j.colsurfa.2021.12 6361.